

Wide-Bandgap Perovskite Quantum Dots in Perovskite Matrix for Sky-Blue Light-Emitting Diodes

Yuan Liu,^{||} Ziliang Li,^{||} Jian Xu,^{||} Yitong Dong, Bin Chen, So Min Park, Dongxin Ma, Seungjin Lee, Jianan Erick Huang, Sam Teale, Oleksandr Voznyy, and Edward H. Sargent*



Cite This: <https://doi.org/10.1021/jacs.1c12556>



Read Online

ACCESS |



Metrics & More

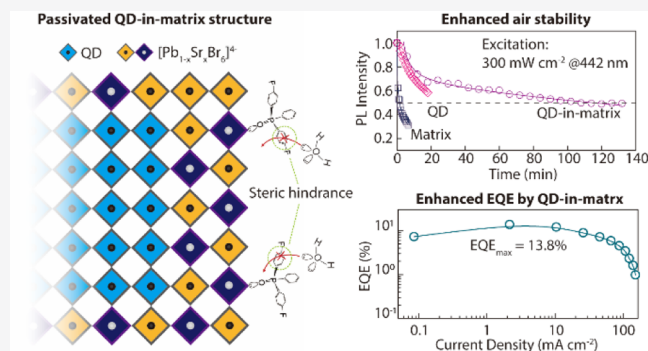


Article Recommendations



Supporting Information

ABSTRACT: The epitaxial growth of a perovskite matrix on quantum dots (QDs) has enabled the emergence of efficient red light-emitting diodes (LEDs) because it unites efficient charge transport with strong surface passivation. However, the synthesis of wide-band gap (E_g) QD-in-matrix heterostructures has so far remained elusive in the case of sky-blue LEDs. Here, we developed CsPbBr₃ QD-in-perovskite matrix solids that enable high luminescent efficiency and spectral stability with an optical E_g of over 2.6 eV. We screened alloy candidates that modulate the perovskite E_g and allow heteroepitaxy, seeking to implement lattice-matched type-I band alignment. Specifically, we introduced a CsPb_{1-x}Sr_xBr₃ matrix, in which alloying with Sr²⁺ increased the E_g of the perovskite and minimized lattice mismatch. We then developed an approach to passivation that would overcome the hygroscopic nature of Sr²⁺. We found that *bis*(4-fluorophenyl)phenylphosphine oxide strongly coordinates with Sr²⁺ and provides steric hindrance to block H₂O, a finding obtained by combining molecular dynamics simulations with experimental results. The resulting QD-in-matrix solids exhibit enhanced air- and photo-stability with efficient charge transport from the matrix to the QDs. LEDs made from this material exhibit an external quantum efficiency of 13.8% and a brightness exceeding 6000 cd m⁻².



INTRODUCTION

Incorporating quantum dots (QDs) into a lead halide perovskite (APbX₃) matrix enables efficient charge transport and surface passivation, leading to efficient and stable optoelectronics.^{1–3} Red light-emitting diodes (LEDs) based on perovskite QD-in-matrix solids have been developed, showing an external quantum efficiency (EQE) of over 18% and an operating lifetime (T_{50}) of over 2000 h at an initial luminance of 100 cd m⁻².⁴ This approach has opened the door for efficient and stable perovskite optoelectronics. In the case of perovskite sky-blue LEDs, both the stability and EQE are still well below the criteria for commercialization.

Strongly confined CsPbBr₃ QDs with an $E_g > 2.55$ eV enable blue emission.^{5,6} Embedding the wide- E_g perovskite QDs into a perovskite matrix thus offers a route toward efficient sky-blue LEDs.

Efficient charge transport in QD-in-matrix solids demands a type-I band alignment between matrix and embedded QDs, requiring the E_g of the matrix to be larger than that of the QDs. Mixing > 30% Cl tunes the E_g of CsPbBr₃-based perovskites above 2.6 eV.^{7,8} However, the high Cl content leads to halide segregation of the mixed Cl/Br perovskite (Figure 1A).⁸ Lattice mismatch between the mixed Cl/Br perovskite matrix (for instance, 5.77 Å for 40% Cl and 5.80 Å for 30% Cl⁹) and

the hygroscopic nature of Sr²⁺. We found that *bis*(4-fluorophenyl)phenylphosphine oxide strongly coordinates with Sr²⁺ and provides steric hindrance to block H₂O, a finding obtained by combining molecular dynamics simulations with experimental results. The resulting QD-in-matrix solids exhibit enhanced air- and photo-stability with efficient charge transport from the matrix to the QDs. LEDs made from this material exhibit an external quantum efficiency of 13.8% and a brightness exceeding 6000 cd m⁻².

CsPbBr₃ QDs (5.87 Å⁶) makes these materials vulnerable to inhomogeneous crystallization due to the epitaxial growth of the [PbBr₆]⁴⁻ octahedron on CsPbBr₃ QDs.^{2,10,11}

We therefore investigated how varying the cation in the perovskite matrix can tune the E_g without introducing lattice distortion. We found that Sr-alloyed perovskites have an $E_g > 2.6$ eV.^{12,13} Meanwhile, because Sr²⁺ and Pb²⁺ have similar sizes,¹⁴ the lattice of the perovskite remains nearly unchanged.

However, the use of Sr²⁺ introduced a chemical challenge: the hygroscopic nature of Sr²⁺ leads to the rapid formation of SrBr₂ · xH₂O in air and the decomposition of the mixed Sr/Pb phase.^{15,16} By uniting molecular dynamics (MD) simulations with experimental results, we found a new passivator, *bis*(4-fluorophenyl)phenylphosphine oxide (DFPPO); DFPPO strongly coordinates with Sr²⁺ cations located on the perovskite surface and offers sufficient steric hindrance to prevent H₂O from invading into the perovskite lattice.

Received: November 29, 2021

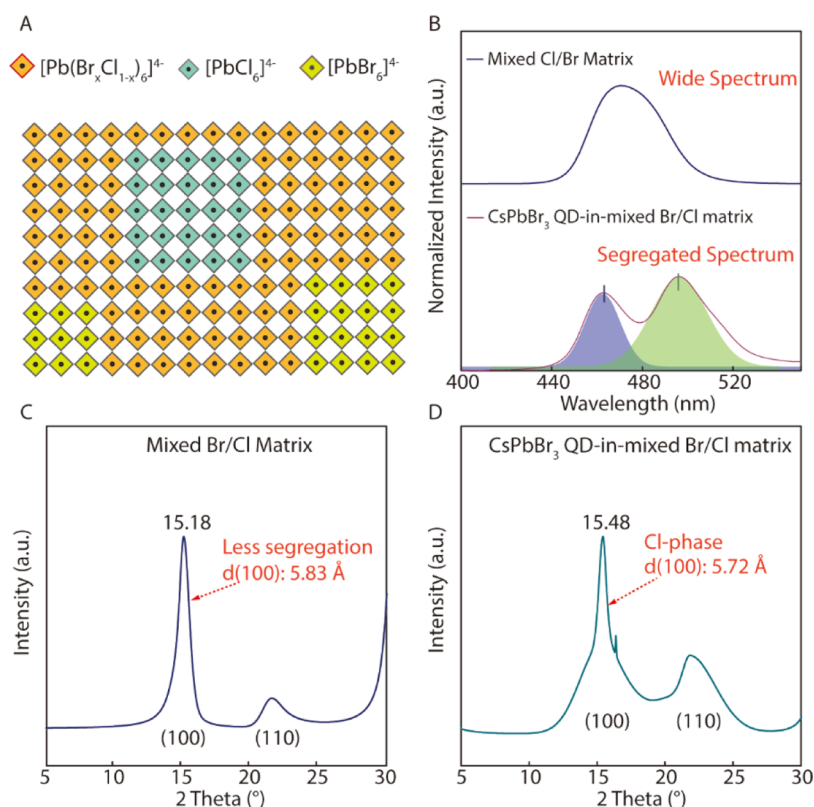


Figure 1. (A) Schematic of halide segregation in mixed Cl/Br perovskites. (B) PL spectra of the mixed Br/Cl perovskite matrix and CsPbBr₃ QD-in-mixed Br/Cl perovskite matrix solids. (C,D) XRD patterns of (C) mixed Br/Cl perovskite matrix and (D) CsPbBr₃ QD-in-mixed Br/Cl matrix.

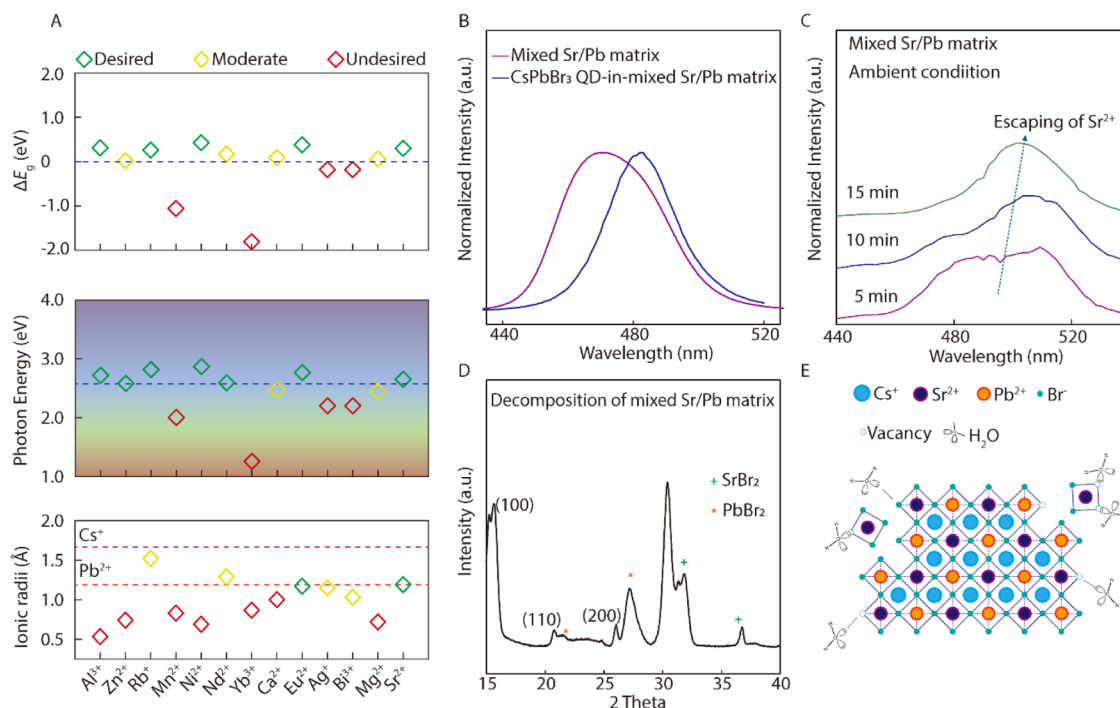


Figure 2. (A) Upper: comparison of the E_g shift induced by alloying. Middle: comparison of the PL photon energy of the resulting materials after being alloyed/doped. Bottom: comparison of the ionic radii of A-site and B-site cation candidates with Pb²⁺ and Cs⁺. (B) PL spectra of mixed Sr/Pb perovskite matrix and QD-in-mixed Sr/Pb perovskite matrix under N₂. (C) PL spectra tracking of the unpassivated mixed Sr/Pb perovskite matrix under ambient conditions. (D) XRD pattern of mixed Sr/Pb perovskite matrix when stored under ambient conditions. (E) Schematic of the dissociation of Sr²⁺ cations as a result of H₂O coordination.

We report as a result air-stable perovskite QD-in-matrix solids that exhibit efficient sky-blue emission (Supporting

Information Figure S1), and we realize LEDs with an EQE of 13.8% and a luminance of over 6 kcd m⁻².

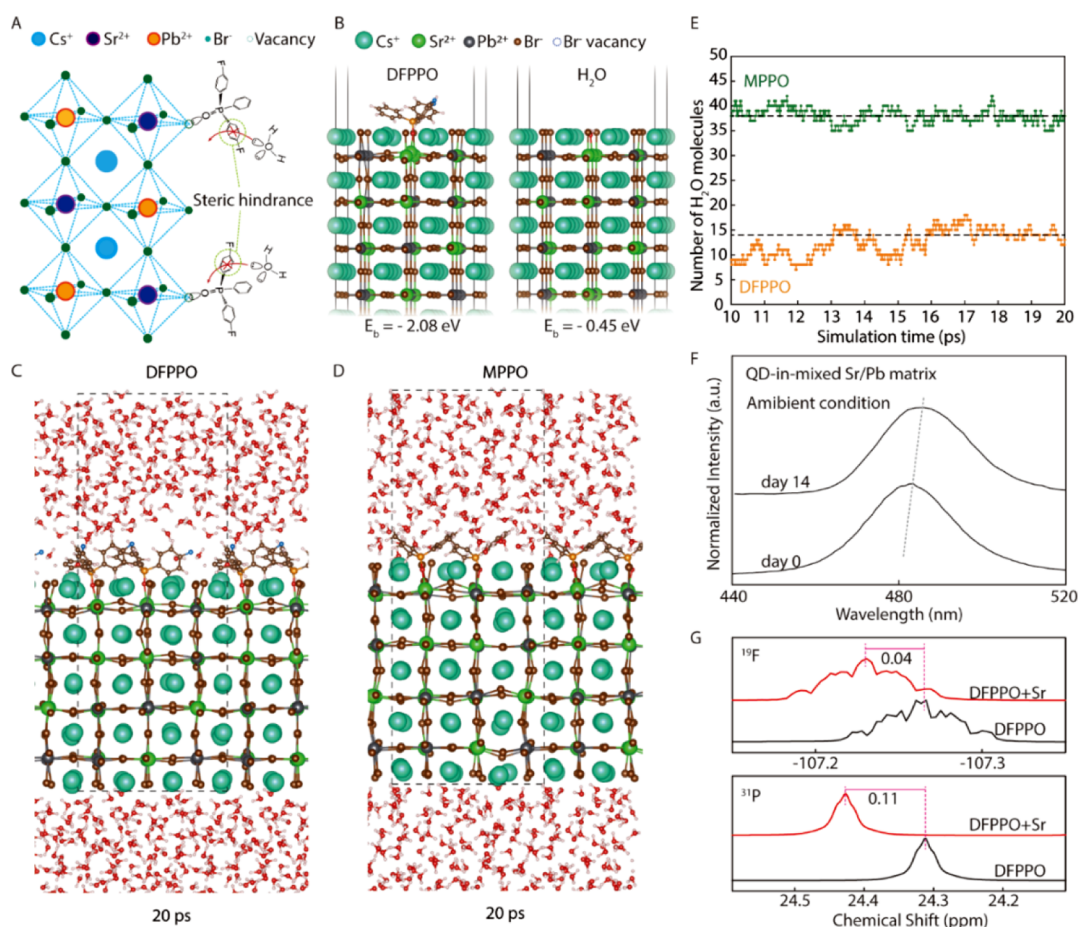


Figure 3. (A) Schematic of Sr^{2+} cations passivated by DFPPO, which offers strong binding and steric hindrance to block H_2O . (B) Binding energy of DFPPO and H_2O with the Sr^{2+} -perovskite surface. Snapshots after 20 ps of MD simulations for the (C) DFPPO- and (D) MPPO-passivated $\text{CsPb}_{0.6}\text{Sr}_{0.4}\text{Br}_3/\text{H}_2\text{O}$ interface. (E) Number of H_2O molecules within 7.5 Å perpendicular distance from the Cs–Br-terminated perovskite surface during the MD simulations for DFPPO- and MPPO-passivated interfaces. (F) PL spectra tracking over 14 days of DFPPO-passivated QD-in-mixed solid stored under ambient conditions. (G) ^{31}P and ^{19}F NMR spectra of DFPPO-Sr and pristine DFPPO.

RESULTS AND DISCUSSION

Seeking to obtain a perovskite matrix with an $E_g > 2.6$ eV, we initially tested a mixed Cl/Br perovskite with 40% Cl content.⁸ However, the resulting films exhibited a broad photoluminescence (PL) spectrum (Figure 1B), indicating the occurrence of phase segregation. When the mixed Cl/Br perovskite was applied as a matrix to QDs, we observed multiple emission peaks ($\lambda_1 \sim 463$ nm and $\lambda_2 \sim 497$ nm, Figure 1B) from the QD-in-matrix films, a finding we attributed to domains with different Cl contents.¹⁷ This agrees with the emergence of an X-ray diffraction (XRD) peak at a high angle ($2\theta = 15.48^\circ$, Figure 1D) in the QD-in-matrix film, which indicates a Cl-rich phase with a smaller lattice parameter [$d(100) \sim 5.72$ Å]. In comparison, the mixed Cl/Br perovskite matrix showed a diffraction peak at 15.18° [Figure 1C, $d(100) \sim 5.83$ Å]. Embedding QDs into the mixed Cl/Br matrix increased the degree of halide segregation, which may be related to the crystallization preference of the Br-rich phase on CsPbBr_3 QDs.

To address the problem, we turned away from the mixed Cl/Br perovskites and investigated A-site and B-site cation alloys to tune the perovskites. We screened cation alloys that are widely used in perovskite materials: Al^{3+} ,¹⁸ Zn^{2+} ,¹⁹ Rb^+ ,²⁰ Mn^{2+} ,²¹ Ni^{2+} ,²² Nd^{2+} ,²³ Yb^{3+} ,²¹ Ca^{2+} ,¹³ Eu^{2+} ,²⁴ Ag^+ ,^{25,26} Bi^{3+} ,^{25,26} Mg^{2+} ,²⁷ and Sr^{2+} .^{12,13} Cation candidates that increase

the E_g of perovskites were selected (Figure 2A). With the goal of minimizing lattice mismatch, we focused on Sr^{2+} in light of its close match with Pb^{2+} in ionic radius (Figure 2A, Supporting Information Figure S2). We screened out Eu^{2+} in light of its low solubility in perovskite precursor solution.²⁸ The resulting QD–matrix combination shows a type-I alignment seen in ultraviolet photoelectron spectroscopy (UPS, Supporting Information Figure S3).

Unfortunately, when we fabricated $\text{CsPb}_{1-x}\text{Sr}_x\text{Br}_3$ perovskite films, we observed that they became green and wet in the air immediately and were readily wiped away (Supporting Information Figure S4A–C). This was accompanied by a red shift in the PL spectrum (Figure 2B,C). Furthermore, XRD patterns of the mixed Sr/Pb perovskite revealed a decomposed thin film containing precursor residues (Figure 2D), an observation we attribute to the dissociation of $[\text{Sr}(\text{H}_2\text{O})_6]^{2+}$.

The Sr^{2+} cations in perovskites are hygroscopic and prone to form $\text{Sr}(\text{H}_2\text{O})_x^{2+}$ in the presence of moisture.^{15,16} H_2O molecules react with $[\text{SrBr}_6]^{4-}$ octahedrons and extract Sr^{2+} cations from the perovskite lattice (Figure 2E).

We therefore pursued the passivation of Sr^{2+} cations in our mixed Sr/Pb perovskite. We posited that Lewis bases (e.g., $\text{S}=\text{O}$, $\text{P}=\text{O}$, and $\text{P}=\text{S}$)^{29–31} that coordinate with Sr^{2+} cations would compete with H_2O . This should also be combined with

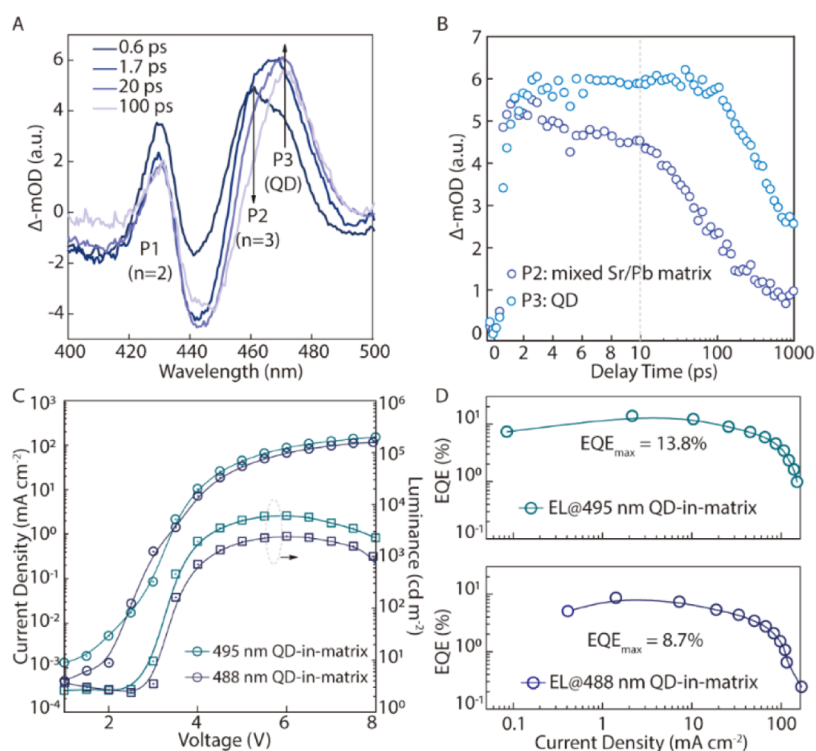


Figure 4. (A) TA spectra of the CsPbBr₃ QD-in-mixed Sr/Pb matrix solid. (B) Kinetic traces of P2 (matrix) and P3 (QD) bleach peaks derived from (A). (C) Representative luminance and current density performance vs applied bias derived from QD-in-mixed Sr/Pb matrix LEDs. (D) EQE, as a function of current density for devices from (C).

large functional groups that offer steric hindrance to H₂O (Figure 3A).

Based on this finding, we chose DFPPPO (Supporting Information Figure S5A), a molecule that contains an electron-donating phosphine oxide group (R₃P=O)²⁹ and large functional groups (4-fluorophenyl and phenyl groups).

From first-principles calculations, we find that DFPPPO has much higher binding energy ($E_b = -2.08$ eV) with the perovskite surface than H₂O ($E_b = -0.45$ eV) (Figure 3B). We also find that DFPPPO has a higher binding energy with Sr²⁺ ($E_b = -2.08$ eV) than with Pb²⁺ ($E_b = -1.51$ eV) on the perovskite surface (Supporting Information Figure S6A). The affinity between DFPPPO and Sr²⁺ cations was testified by recording chemical shifts (δ) in ³¹P and ¹⁹F nuclear magnetic resonance (NMR) measurement. The δ values increased upon mixing Sr²⁺ with DFPPPO solution (Figure 3G), which is higher than that of other perovskite precursors (Supporting Information Figure S7A).

We compared the E_b with two other molecules that contain smaller functional groups, 3-methyl-1-phenyl-2-phospholene 1-oxide (MPPO) and (2-ethoxyethyl)(diphenyl)phosphine oxide (EDPO) (Supporting Information Figure S5B,C). DFPPPO exhibited stronger binding with Sr²⁺ than EDPO ($E_b = -1.79$ eV) and MPPO ($E_b = -1.95$ eV) (Supporting Information Figure S6B,C, NMR results in Supporting Information Figure S7B,C).

To further verify the role that steric hindrance plays in the passivation against water degradation, we performed MD simulations for the interface of the ligand-passivated perovskite/H₂O. We find that fewer H₂O molecules penetrate the perovskite layer in the DFPPPO-passivated system compared with MPPO (Figure 3C,D). We show the number of H₂O molecules within 7.5 Å perpendicular distance from the Cs–

Br-terminated perovskite surface during the MD simulations (Figure 3E). There are 14 and 38 H₂O molecules on average (between 15 and 20 ps) located in this height region for DFPPPO- and MPPO-passivated perovskites, respectively.

We offer that DFPPPO provides increased steric hindrance that helps to prevent H₂O from invading into the perovskite lattice. We also found that no degradation occurred in the mixed Sr/Pb perovskite when using triphenylphosphine oxide (TPPO), a structural analogue of DFPPPO (Supporting Information Figures S5D, S8A).

The resulting DFPPPO-passivated mixed Sr/Pb perovskite exhibited stable emission at 482 nm. The films showed a PL shift of less than 5 nm when stored under ambient conditions over 14 days (relative humidity = 15%, used in all PL measurements under ambient conditions; Figure 3F), indicating that nearly no degradation occurred. The addition of DFPPPO molecules also improved the stability of the mixed Sr/Pb perovskite thin films under intense excitation (Supporting Information Figure S9), a common attribute of a defect- and degradation-free material. XRD patterns demonstrated that the perovskite structure was retained and no precursor peaks arose (Supporting Information Figure S10A). Although MPPO and EDPO exhibit comparably high binding energy, severe phase degradation was observed in the thin films using MPPO and EDPO for passivation: multiple PL peaks arose when these thin films were exposed to air (Supporting Information Figures S4E, S8B,C). These results support the prediction from the MD simulations that H₂O molecules penetrate through small passivants and react with Sr²⁺ cations.

To acquire the structural information of the QD-in-matrix solid, we carried out high-resolution transmission electron microscopy. The QDs have a diameter of ~4.2 nm and are surrounded by a perovskite matrix (Supporting Information

Figure S11A). Both the QD and matrix show clear lattice patterns and similar patterns in fast Fourier transform images, agreeing with the possibility of heteroepitaxy (Supporting Information Figure S11C,D). The matrix-only perovskite shows featureless perovskite flakes, while CsPbBr₃ QDs show isolated particles (Supporting Information Figure S11E,F). We further measured *in situ* PL during spin coating: intense PL emerged immediately after we deposited QDs on the matrix solution, supporting the view that QDs remained intact in the matrix solution (Supporting Information Figure S12A,B). The PL is retained in the resulting QD-in-matrix solid following methyl acetate rinsing, which is attributed to the protection of the matrix (Supporting Information Figure S12C,D). XRD patterns of the QD-in-matrix solid reveal a decomposition-free film (Supporting Information Figure S10B) and nearly identical lattice parameters of the QDs and matrix (Supporting Information Figure S10C).

To investigate charge transport and surface passivation in QD-in-matrix solids, we employed transient absorption (TA) and PL lifetime measurements. We observed bleach peaks in TA spectra at 430 nm (P1), 460 nm (P2), and 472 nm (P3) in the QD-in-mixed Sr/Pb matrix samples (Figure 4A). We assign these to the band-edge bleach of the matrix (P1 and P2) and QDs (P3). The emergence of multiple bleach peaks (P1 and P2) is related to the domain size mixing in 2.5 D perovskites that we used as the matrix. The bleach recovery dynamics of P2 and P3 (Figure 4B) show increasing peak amplitude of P3 (QD) accompanied by fast recovery of P2 (matrix) in the first 4 ps. This agrees with population transfer from P2 to P3 (Figure 4A). Similar charge transfer processes were observed previously in chalcogenide QD-in-matrix and perovskite QD-in-matrix studies,^{2,4} in which charges were funneled through the wide-*E_g* matrix to the low-*E_g* QDs. Meanwhile, the longer bleach recovery time of P3 suggests a high-quality QD-matrix interface (Figure 4B). Compared with pristine QDs passivated by bipolar ligands, the QD-in-matrix solids show longer PL lifetimes, again consistent with the surface passivation of the QDs by the matrix (Supporting Information Figure S13).

We then fabricated LEDs based on the new QD-in-matrix material, using an ITO/PEDOT:PSS:PFI (PEPFI)/QD-in-matrix solid/TPBi/LiF/Al (Supporting Information Figure S14A) device structure. PEPFI is chosen as the hole transport layer (HTL) considering its hole injection capability and polar solvent compatibility with the matrix precursor solution. However, an undesired red shift arose when we processed the matrix films on PEPFI (Supporting Information Figure S15), a finding we attribute to the ionic nature of the PEPFI surface.^{7,31,32} In order to maintain type-I band alignment, we revised the synthesis of the QDs by increasing the temperature at which hot injection was carried out (details in Method), shifting their PL emission to >485 nm.

LEDs based on smaller QDs exhibited an electroluminescence (EL) maximum at 488 nm, a maximum luminance of ~2400 cd m⁻², and an EQE of 8.7%. Devices using larger QDs showed an EL maximum at 495 nm, a maximum luminance of 6113 cd m⁻², and an EQE of 13.8% (Figure 4C,D). In comparison, QD-only devices showed an EQE of 0.5% and a luminance of ~400 cd m⁻²; matrix-only devices showed an EQE of 0.2% and a luminance of ~40 cd m⁻² (Supporting Information Figure S14B–D).

We further studied the stability of the QD-in-matrix solid by tracking PL under intense laser illumination (300 mW cm⁻² CW laser @445 nm) and ambient conditions. The QD-in-

matrix solid is resistant to PL shifting (Supporting Information Figure S16B,C, ~5 nm after *T*₅₀ = 140 min) while QD-only and matrix-only samples suffered from rapid decay in PL intensity in the first 6 and 30 min, respectively (Supporting Information Figure S16A,C). We attribute these results to the surface protection of the QD by the matrix and the efficient charge funneling into the QDs that reduces charge accumulation in the matrix.^{4,33} The QD-in-matrix LEDs retain their emission wavelength when we increase bias to 12 V (Supporting Information Figure S17A) and exhibit enhanced EL stability (*T*₅₀) compared with the QD-only devices (relative humidity = 17%, used in all LED measurements. Supporting Information Figure S17B; matrix-only devices do not reach 100 cd m⁻² luminance).

CONCLUSIONS

We developed air-stable mixed Sr/Pb perovskites as matrix materials for CsPbBr₃ QDs and fabricated wide-*E_g* perovskite QD-in-matrix solids for sky-blue LEDs. The perovskite QD-in-matrix solids implement a type-I band alignment and lattice matching between the QD and the matrix. To overcome the hygroscopic nature of Sr²⁺ cations, we passivated the mixed Sr/Pb perovskite matrix using DFPPPO molecules that offer strong binding with the Sr²⁺ cations and sufficient steric hindrance to block H₂O. Efficient and spectra-stable LEDs were fabricated based on the QD-in-matrix solid. Furthermore, studies are required to develop HTLs with improved charge injection capability and perovskite crystallization compatibility.

EXPERIMENTAL SECTION

CsPbBr₃ QD Synthesis and Purification. Quantum-confined size-tunable CsPbBr₃ QDs were synthesized and purified following a previously reported method.⁵ Cs precursors were prepared by loading 300 mg of Cs₂CO₃, 1.2 mL of oleic acid (OAc), and 3.2 mL of 1-octadecene (ODE) in a three-necked round-bottom flask under nitrogen. Then, the Cs precursors were dried at room temperature for 10 min and dissolved at 150 °C under N₂ atmosphere. The solution was kept under 120 °C before use.

For 480 nm QDs, 600 mg of PbBr₂ and 1400 mg of ZnBr₂ were loaded in a 250 mL flask together with 14 mL of OAc, 14 mL of oleylamine (OAm), and 40 mL of ODE. The solution was subsequently stirred and dried at 100 °C until no residual could be found. Then, the solution was slowly cooled down under N₂ until 80 °C when 2.7 mL of the Cs precursor was swiftly injected. The solution was kept at 80 °C for 3 min to complete the reaction and quenched in an ice bath. The obtained solution was centrifuged and kept at room temperature for 24 h before purification. The still solution was centrifuged again, and the supernatant was kept for purification.

The nanoparticles were obtained by adding acetone with a volume ratio of 1:1 to the solution, followed by centrifugation at 7800 rpm for 3 min. All the particles were redissolved in 7 mL of toluene and stored in a fridge.

Synthesis and purification of 485 and 490 nm QDs follow a similar procedure, where 700 mg of PbBr₂ was loaded in the precursor solution instead. The injection temperatures are 85 and 95 °C for 485 and 490 nm QDs, respectively.

CsPbBr₃ QD Ligand Exchange. CsPbBr₃ QD ligand exchange follows a previously reported method.⁶ The QD solution was stored in a fridge for over 24 h before use and was centrifuged again before ligand exchange. Then, the QDs were precipitated with 20 mL of methyl acetate and redissolved in 5 mL of toluene. Then, ~120 μL of 200 mg/mL IPABr DMF solution was added to the mixture. The solution was vortexed for 1 min and centrifuged at 7800 rpm for 1 min to remove exchanged and excessive ligands. The QDs were precipitated again with 20 mL of methyl acetate and redissolved in 5 mL of toluene.

To keep a bromine-rich surface for matrix–perovskite shelling, ~ 80 μL of NaBr saturated DMF solution was added for additional exchange. QDs were purified again following the abovementioned steps. The final QD precipitants were dissolved in 1.5 mL of DFPPPO–toluene solution (10 mg mL^{-1}) followed by centrifuging at 15,000 rpm. The exchanged QDs were immediately used for making QD-in-matrix solids.

The final concentration of QDs was estimated by measuring the optical density of the solution at 400 nm using previously reported data of CsPbBr₃ QD cross-sections.³⁴ The final QD concentration was around 38–43 μM .

Preparation of Mixed Sr/Pb Reduced-Dimensional Perovskite Precursors. Reduced-dimensional perovskite precursor solutions were prepared by dissolving PbBr₂, SrBr₂, MABr, CsBr, and PEABr in DMSO with a Pb + Sr concentration of 0.3 M. In detail, for 40% Sr and $n = 3$ matrix shell, 0.36 mmol of PbBr₂, 0.24 mmol of SrBr₂, 0.32 mmol of CsBr, 15 mg of MABr, and 0.4 mmol of PEABr were mixed and dissolved in 2 mL of DMSO in a nitrogen-filled glovebox with continuous stirring for over 120 min. Mixed Cl/Br precursors were prepared with a chemical formula $\text{PEA}_2(\text{Cs}_{0.8}\text{MA}_{0.2})_2\text{Pb}_3(\text{Br}_{1-x}\text{Cl}_x)_{10}$ while keeping a Pb concentration of 0.4 M. All solutions were filtrated using 0.45 μm PTFE filters before use.

Fabrication of QD-in-Matrix Solid and LEDs. 120 μL of precursor solution was spin-cast by a two-step process at 1000 rpm for 10 s and 5000 rpm for 30 s, sequentially. 150 μL of QD solution was then dripped on the precursor solution at 25 s in the second step of spin casting to obtain a QD-dispersed saturated precursor solution film. Films were kept initially at 50 °C for ~ 30 s for controlled crystallization and annealed at 100 °C for another 5 min. For matrix-only films, antisolvent (toluene herein) solely containing 10 mg mL⁻¹ DFPPPO was used instead of a QD solution; all steps are the same for preparing QD-in-matrix solid.

For LED fabrication, ITO/glass substrates were cleaned using deionized water, acetone, and 2-propanol sequentially using ultrasonic cleaners and dried. PEDOT:PSS solution was mixed with PFI solution at a mass ratio of 1:0.99 under continuous stirring for 1 h. Filtered (using 0.45 μm polyvinylidene difluoride filters) PEDOT:PSS:PFI solution was spin-coated on the O-plasma-treated ITO substrate following a two-step recipe (500 rpm for 10 s followed by 4500 rpm for 90 s). The PEDOT:PSS:PFI films were baked at 150 °C under ambient conditions for 15–30 min.

Deposition of active layers was conducted in a nitrogen-filled glovebox. QD-in-matrix and matrix-only films were coated following the abovementioned recipe. Before depositing QD-only films, PVK (4 mg mL⁻¹ in chlorobenzene) was spin-coated on the PEDOT:PSS:PFI substrate (3000 rpm for 30 s), followed by annealing at 125 °C for 15 min. Then, a 10 mg mL⁻¹ PEABr solution was deposited on PVK (4000 rpm for 30 s), immediately followed by deposition of QD solution (3000 rpm 30 s). The as-prepared QD films were annealed at 80 °C for 5 min.

Then, 40 nm TPBi, 1 nm LiF, and 90 nm Al were deposited on the active layers in a thermal evaporation chamber under a high vacuum ($<10^{-7}$ Torr). All the devices were encapsulated using Scotch tapes.

LED Performance and Stability Measurement. The J – V characteristics of LEDs were recorded using a Keithley 647 source meter. EL spectra and luminance at a certain J – V point were measured using a calibrated fiber-coupled spectrometer (QE-pro, Ocean Optics) and an integrating sphere.

UPS Measurements. UPS measurement was performed at nanoFAB, University of Alberta (Canada), using a Kratos Axis Ultra spectrometer. UPS was performed with a He I source ($h\nu = 21.2\text{ eV}$). The sample was measured under -10 V bias. The power for UPS was 3 kV \times 20 mA (60 W).

TA Measurements. TA spectra were collected using a femto-second (fs) pump–probe spectroscopy system. The fs laser pulses were produced using a regeneratively amplified Yb:KGW laser (Light Conversion, Pharos) at a 1 kHz repetition rate. The pump pulse was generated by passing through an optical parametric amplifier (OPA, light conversion orpheus) and chopped, while the other portion of the

fundamental beam was directed on a sapphire crystal after focusing to generate a white light supercontinuum as the probe light. The power of the pump light was measured using a power meter (Ophir) to ensure that the excitation fluence was below the Auger threshold. The time delay of the probe pulses was optically controlled with a translation stage. The probe light spectra were collected with a CCD detector. TA bleach recovery dynamics were recorded at the band-edge bleach peak position.

X-Ray Diffraction Measurement. XRD patterns were obtained using a benchtop X-ray diffractometer (Miniflex, Rigaku). For QD powder preparation, QDs were purified twice with methyl acetate and eventually dissolved in 1.5 mL of toluene. QD solution was then deposited on a substrate dropwise until fully dried.

Steady-State and Time-Resolved PL Measurement. PL spectra and PLQY were measured and calculated using a HORIBA Fluorolog system coupled with a xenon lamp. High-power excited, time-resolved PL intensity tracking was conducted by using a CW laser (442 nm) and a fiber-coupled spectrometer (QE-pro, Ocean Optics) under ambient conditions.

TEM Measurement. Samples for TEM imaging were prepared by using the same spin coating and annealing method above with a copper TEM grid. TEM was performed using a Hitachi HF-3300 S/TEM system, operated at 300 kV.

NMR Measurement. Samples for NMR measurement were prepared by dissolving DFPPPO (10 mg mL⁻¹) alone and with SrBr₂ (10 mg mL⁻¹) (same for MPPPO, EDPO, PbBr₂, MABr, and PEABr samples) in DMSO-*d*₆. 1D 19F NMR (19F; 470.30 MHz), and 1D 31P NMR (31P; 202.35 MHz) spectra were acquired at 25 °C using a 500 MHz Agilent DD2 spectrometer equipped with a 5 mm 1H–19F{X} OneNMR probe. The spectra were acquired using the standard phosphorus pulse sequence as supplied by Varian/Agilent acquisition software.

DFT Calculation. First-principles calculations based on density functional theory (DFT) were carried out using the Vienna Ab initio Simulation Package (VASP).³⁵ The generalized gradient approximation (GGA) of the Perdew–Burke–Ernzerhof (PBE) functional was employed as the exchange–correlation functional.³⁶ The DFT-D3 method for the van der Waals (vdW) correction was included.³⁷ The plane-wave cutoff energy was 400 eV. The energy and force convergence criteria were set to 10⁻⁵ eV and 0.02 eV·Å⁻¹, respectively. The Γ -centered $2 \times 2 \times 1$ k-mesh was used in the surface slab calculations. The binding energies (E_b) of ligands with the perovskite surface were calculated as $E(\text{ligand@perovskite}) - E(\text{ligand}) - E(\text{perovskite})$, where $E(\text{structure})$ is the total energy of the corresponding structure.

Molecular Dynamics Simulations. Ab-initio molecular dynamics simulations (AIMD) were performed with the CP2K package³⁸ in the constant-volume and constant-temperature (NVT) ensemble. The target temperature was set to 300 K with a Nosé–Hoover thermostat.³⁹ The PBE-D3 functional was used with double-zeta basis sets (DZVP-MOLOPT)⁴⁰ and Goedecker–Teter–Hutter (GTH) pseudopotentials.⁴¹ The cutoff was set to 560 Ry. We constructed the CsPb_{0.6}Sr_{0.4}Br₃/H₂O interface model with a (3 \times 3) supercell and a 15 Å-thick H₂O layer, employing the experimental density of liquid water. The AIMD simulations are run for 20 ps with a 1.0 fs time step.

■ ASSOCIATED CONTENT

Supporting Information

The Supporting Information is available free of charge at <https://pubs.acs.org/doi/10.1021/jacs.1c12556>.

Materials, CIE coordinates, size comparison of A-site and B-site alloy candidates, UPS measurements of QD and matrix, images of mixed Sr/Pb perovskites, molecular structures, binding energy, ³¹P and ¹⁹F NMR spectra, PL spectra, XRD pattern, HRTEM images, in-situ PL tracking, device architecture of the QD-in-matrix LEDs, TA spectra, PL tracking under

intense excitation, and EL spectral stability of devices
(PDF)

AUTHOR INFORMATION

Corresponding Author

Edward H. Sargent – Department of Electrical and Computer Engineering, University of Toronto, Toronto M5S 1A4, Canada; orcid.org/0000-0003-0396-6495; Email: ted.sargent@utoronto.ca

Authors

Yuan Liu – Department of Electrical and Computer Engineering, University of Toronto, Toronto M5S 1A4, Canada; orcid.org/0000-0001-8611-1673

Ziliang Li – Department of Electrical and Computer Engineering, University of Toronto, Toronto M5S 1A4, Canada; orcid.org/0000-0002-3300-4759

Jian Xu – Department of Electrical and Computer Engineering, University of Toronto, Toronto M5S 1A4, Canada; orcid.org/0000-0002-1532-5145

Yitong Dong – Department of Electrical and Computer Engineering, University of Toronto, Toronto M5S 1A4, Canada; Present Address: Department of Chemistry and Biochemistry, University of Oklahoma, Norman, OK 73019, United States

Bin Chen – Department of Electrical and Computer Engineering, University of Toronto, Toronto M5S 1A4, Canada; orcid.org/0000-0002-2106-7664

So Min Park – Department of Electrical and Computer Engineering, University of Toronto, Toronto M5S 1A4, Canada

Dongxin Ma – Department of Electrical and Computer Engineering, University of Toronto, Toronto M5S 1A4, Canada; orcid.org/0000-0002-9790-5951

Seungjin Lee – Department of Electrical and Computer Engineering, University of Toronto, Toronto M5S 1A4, Canada; orcid.org/0000-0002-6318-0702

Jianan Erick Huang – Department of Electrical and Computer Engineering, University of Toronto, Toronto M5S 1A4, Canada

Sam Teale – Department of Electrical and Computer Engineering, University of Toronto, Toronto M5S 1A4, Canada; orcid.org/0000-0001-9638-3453

Oleksandr Voznyy – Department of Physical and Environmental Sciences, University of Toronto, Toronto M1C 1A4, Canada; orcid.org/0000-0002-8656-5074

Complete contact information is available at:
<https://pubs.acs.org/10.1021/jacs.1c12556>

Author Contributions

[†]Y.L., Z.L., and J.X. contributed equally.

Notes

The authors declare no competing financial interest.

ACKNOWLEDGMENTS

This work was supported by the Natural Sciences and Engineering Research Council of Canada (NSERC, grant number 537463-18). The authors acknowledge Huawei Canada for its financial support. Electron microscopy was performed at the Ontario Center for the characterization of advanced materials, funded by the Canada Foundation for Innovation (CFI).

REFERENCES

- (1) Gao, L.; Quan, L. N.; García de Arquer, F. P.; Zhao, Y.; Munir, R.; Proppe, A.; Quintero-Bermudez, R.; Zou, C.; Yang, Z.; Saidaminov, M. I.; Voznyy, O.; Kinge, S.; Lu, Z.; Kelley, S. O.; Amassian, A.; Tang, J.; Sargent, E. H. Efficient Near-Infrared Light-Emitting Diodes Based on Quantum Dots in Layered Perovskite. *Nat. Photonics* **2020**, *14*, 227–233.
- (2) Ning, Z.; Gong, X.; Comin, R.; Walters, G.; Fan, F.; Voznyy, O.; Yassitepe, E.; Buin, A.; Hoogland, S.; Sargent, E. H. Quantum-Dot-in-Perovskite Solids. *Nature* **2015**, *523*, 324–328.
- (3) Quintero-Bermudez, R.; Sabatini, R. P.; Lejay, M.; Voznyy, O.; Sargent, E. H. Small-Band-Offset Perovskite Shells Increase Auger Lifetime in Quantum Dot Solids. *ACS Nano* **2017**, *11*, 12378–12384.
- (4) Liu, Y.; Dong, Y.; Zhu, T.; Ma, D.; Proppe, A.; Chen, B.; Zheng, C.; Hou, Y.; Lee, S.; Sun, B.; Jung, E. H.; Yuan, F.; Wang, Y.-k.; Sagar, L. K.; Hoogland, S.; García de Arquer, F. P.; Choi, M.-J.; Singh, K.; Kelley, S. O.; Voznyy, O.; Lu, Z.-H.; Sargent, E. H. Bright and Stable Light-Emitting Diodes Based on Perovskite Quantum Dots in Perovskite Matrix. *J. Am. Chem. Soc.* **2021**, *143*, 15606–15615.
- (5) Dong, Y.; Qiao, T.; Kim, D.; Parobek, D.; Rossi, D.; Son, D. H. Precise Control of Quantum Confinement in Cesium Lead Halide Perovskite Quantum Dots via Thermodynamic Equilibrium. *Nano Lett.* **2018**, *18*, 3716–3722.
- (6) Dong, Y.; Wang, Y.-K.; Yuan, F.; Johnston, A.; Liu, Y.; Ma, D.; Choi, M.-J.; Chen, B.; Chekini, M.; Baek, S.-W.; Sagar, L. K.; Fan, J.; Hou, Y.; Wu, M.; Lee, S.; Sun, B.; Hoogland, S.; Quintero-Bermudez, R.; Ebe, H.; Todorovic, P.; Dinic, F.; Li, P.; Kung, H. T.; Saidaminov, M. I.; Kumacheva, E.; Spiecker, E.; Liao, L.-S.; Voznyy, O.; Lu, Z.-H.; Sargent, E. H. Bipolar-Shell Resurfacing for Blue LEDs Based on Strongly Confined Perovskite Quantum Dots. *Nat. Nanotechnol.* **2020**, *15*, 668–674.
- (7) Ma, D.; Todorović, P.; Meshkat, S.; Saidaminov, M. I.; Wang, Y.-K.; Chen, B.; Li, P.; Scheffel, B.; Quintero-Bermudez, R.; Fan, J. Z.; Dong, Y.; Sun, B.; Xu, C.; Zhou, C.; Hou, Y.; Li, X.; Kang, Y.; Voznyy, O.; Lu, Z.-H.; Ban, D.; Sargent, E. H. Chloride Insertion–Immobilization Enables Bright, Narrowband, and Stable Blue-Emitting Perovskite Diodes. *J. Am. Chem. Soc.* **2020**, *142*, 5126–5134.
- (8) Karlsson, M.; Yi, Z.; Reichert, S.; Luo, X.; Lin, W.; Zhang, Z.; Bao, C.; Zhang, R.; Bai, S.; Zheng, G.; Teng, P.; Duan, L.; Lu, Y.; Zheng, K.; Pullerits, T.; Deibel, C.; Xu, W.; Friend, R.; Gao, F. Mixed Halide Perovskites for Spectrally Stable and High-Efficiency Blue Light-Emitting Diodes. *Nat. Commun.* **2021**, *12*, 361.
- (9) Cha, J.-H.; Noh, K.; Yin, W.; Lee, Y.; Park, Y.; Ahn, T. K.; Mayoral, A.; Kim, J.; Jung, D.-Y.; Terasaki, O. Formation and Encapsulation of All-Inorganic Lead Halide Perovskites at Room Temperature in Metal-Organic Frameworks. *J. Phys. Chem. Lett.* **2019**, *10*, 2270–2277.
- (10) Liu, J.; Zhang, J. Nanointerface Chemistry: Lattice-Mismatch-Directed Synthesis and Application of Hybrid Nanocrystals. *Chem. Rev.* **2020**, *120*, 2123–2170.
- (11) Peng, X.; Schlamp, M. C.; Kadavanich, A. V.; Alivisatos, A. P. Epitaxial Growth of Highly Luminescent CdSe/CdS Core/Shell Nanocrystals with Photostability and Electronic Accessibility. *J. Am. Chem. Soc.* **1997**, *119*, 7019–7029.
- (12) Cai, L.; Liang, D.; Wang, X.; Zang, J.; Bai, G.; Hong, Z.; Zou, Y.; Song, T.; Sun, B. Efficient and Bright Pure-Blue All-Inorganic Perovskite Light-Emitting Diodes from an Ecofriendly Alloy. *J. Phys. Chem. Lett.* **2021**, *12*, 1747–1753.
- (13) Li, J.; Wang, X.; Tan, Y.; Liang, D.; Zou, Y.; Cai, L.; Wu, T.; Wen, K.; Wang, Y.; Li, Y.; Song, T.; Wang, L.; Sun, B. Strontium Ion B-Site Substitution for Spectral-Stable Blue Emitting Perovskite Light-Emitting Diodes. *Adv. Opt. Mater.* **2020**, *8*, 2001073.
- (14) Shannon, R. D. Revised Effective Ionic Radii and Systematic Studies of Interatomic Distances in Halides and Chalcogenides. *Acta Crystallogr., Sect. A: Cryst. Phys., Diff., Theor. Gen. Crystallogr.* **1976**, *32*, 751–767.
- (15) Loyd, M.; Lindsey, A.; Patel, M.; Koschan, M.; Melcher, C. L.; Zhuravleva, M. Crystal Structure and Thermal Expansion of

CsCaI₃:Eu and CsSrBr₃:Eu Scintillators. *J. Cryst. Growth* **2018**, *481*, 35–39.

(16) Jacobsson, T. J.; Pazoki, M.; Hagfeldt, A.; Edvinsson, T. Goldschmidt's Rules and Strontium Replacement in Lead Halogen Perovskite Solar Cells: Theory and Preliminary Experiments on CH₃NH₃SrI₃. *J. Phys. Chem. C* **2015**, *119*, 25673–25683.

(17) Cho, J.; Kamat, P. V. Photoinduced Phase Segregation in Mixed Halide Perovskites: Thermodynamic and Kinetic Aspects of Cl–Br Segregation. *Adv. Opt. Mater.* **2020**, *9*, 2001440.

(18) Liu, M.; Zhong, G.; Yin, Y.; Miao, J.; Li, K.; Wang, C.; Xu, X.; Shen, C.; Meng, H. Aluminum-Doped Cesium Lead Bromide Perovskite Nanocrystals with Stable Blue Photoluminescence Used for Display Backlight. *Adv. Sci.* **2017**, *4*, 1700335.

(19) Thapa, S.; Adhikari, G. C.; Zhu, H.; Grigoriev, A.; Zhu, P. Zn-Alloyed All-Inorganic Halide Perovskite-Based White Light-Emitting Diodes with Superior Color Quality. *Sci. Rep.* **2019**, *9*, 18636.

(20) Jiang, Y.; Qin, C.; Cui, M.; He, T.; Liu, K.; Huang, Y.; Luo, M.; Zhang, L.; Xu, H.; Li, S.; Wei, J.; Liu, Z.; Wang, H.; Kim, G. H.; Yuan, M.; Chen, J. Spectra Stable Blue Perovskite Light-Emitting Diodes. *Nat. Commun.* **2019**, *10*, 1868.

(21) Cai, T.; Wang, J.; Li, W.; Hills-Kimball, K.; Yang, H.; Nagaoka, Y.; Yuan, Y.; Zia, R.; Chen, O. Mn²⁺/Yb³⁺. Codoped CsPbCl₃ Perovskite Nanocrystals with Triple-Wavelength Emission for Luminescent Solar Concentrators. *Adv. Sci.* **2020**, *7*, 2001317.

(22) Pan, G.; Bai, X.; Xu, W.; Chen, X.; Zhai, Y.; Zhu, J.; Shao, H.; Ding, N.; Xu, L.; Dong, B.; Mao, Y.; Song, H. Bright Blue Light Emission of Ni²⁺ Ion-Doped CsPbCl_{3-x} Perovskite Quantum Dots Enabling Efficient Light-Emitting Devices. *ACS Appl. Mater. Interfaces* **2020**, *12*, 14195–14202.

(23) Chiba, T.; Sato, J.; Ishikawa, S.; Takahashi, Y.; Ebe, H.; Sumikoshi, S.; Ohisa, S.; Kido, J. Neodymium Chloride-Doped Perovskite Nanocrystals for Efficient Blue Light-Emitting Devices. *ACS Appl. Mater. Interfaces* **2020**, *12*, 53891–53898.

(24) Luo, J.; Yang, L.; Tan, Z.; Xie, W.; Sun, Q.; Li, J.; Du, P.; Xiao, Q.; Wang, L.; Zhao, X.; Niu, G.; Gao, L.; Jin, S.; Tang, J. Efficient Blue Light Emitting Diodes Based On Europium Halide Perovskites. *Adv. Mater.* **2021**, *33*, 2101903.

(25) Du, K.-z.; Wang, X.; Han, Q.; Yan, Y.; Mitzi, D. B. Heterovalent B-Site Co-Alloying Approach for Halide Perovskite Bandgap Engineering. *ACS Energy Lett.* **2017**, *2*, 2486–2490.

(26) Liu, Y.; Zhang, L.; Wang, M.; Zhong, Y.; Huang, M.; Long, Y.; Zhu, H. Bandgap-Tunable Double-Perovskite Thin Films by Solution Processing. *Mater. Today* **2019**, *28*, 25–30.

(27) Adhikari, G. C.; Thapa, S.; Zhu, H.; Zhu, P. Mg²⁺-Alloyed All-Inorganic Halide Perovskites for White Light-Emitting Diodes by 3D-Printing Method. *Adv. Opt. Mater.* **2019**, *7*, 1900916.

(28) Huang, J.; Lei, T.; Siron, M.; Zhang, Y.; Yu, S.; Seeler, F.; Dehestani, A.; Quan, L. N.; Schierle-Arndt, K.; Yang, P. Lead-Free Cesium Europium Halide Perovskite Nanocrystals. *Nano Lett.* **2020**, *20*, 3734–3739.

(29) Haake, P.; Cook, R. D.; Hurst, G. H. Evaluation of the Basicity of Phosphine Oxides and Phosphine Sulfides by Measurements of Chemical Shift in Sulfuric Acid Solutions. *J. Am. Chem. Soc.* **1967**, *89*, 2650–2654.

(30) Cotton, F. A.; Francis, R. Sulfoxides as Ligands. I. A Preliminary Survey of Methyl Sulfoxide Complexes. *J. Am. Chem. Soc.* **1960**, *82*, 2986–2991.

(31) Ma, D.; Lin, K.; Dong, Y.; Choubisa, H.; Proppe, A. H.; Wu, D.; Wang, Y.-K.; Chen, B.; Li, P.; Fan, J. Z.; Yuan, F.; Johnston, A.; Liu, Y.; Kang, Y.; Lu, Z.-H.; Wei, Z.; Sargent, E. H. Distribution Control Enables Efficient Reduced-Dimensional Perovskite LEDs. *Nature* **2021**, *599*, 594–598.

(32) Xing, J.; Zhao, Y.; Askerka, M.; Quan, L. N.; Gong, X.; Zhao, W.; Zhao, J.; Tan, H.; Long, G.; Gao, L.; Yang, Z.; Voznyy, O.; Tang, J.; Lu, Z.-H.; Xiong, Q.; Sargent, E. H. Color-Stable Highly Luminescent Sky-Blue Perovskite Light-Emitting Diodes. *Nat. Commun.* **2018**, *9*, 3541.

(33) Draguta, S.; Sharia, O.; Yoon, S. J.; Brennan, M. C.; Morozov, Y. V.; Manser, J. S.; Kamat, P. V.; Schneider, W. F.; Kuno, M.

Rationalizing the Light-Induced Phase Separation of Mixed Halide Organic–Inorganic Perovskites. *Nat. Commun.* **2017**, *8*, 200.

(34) Puthenpurayil, J.; Cheng, O. H.-C.; Qiao, T.; Rossi, D.; Son, D. H. On the Determination of Absorption Cross Section of Colloidal Lead Halide Perovskite Quantum Dots. *J. Chem. Phys.* **2019**, *151*, 154706.

(35) Kresse, G.; Furthmüller, J. Efficient Iterative Schemes for Ab Initio Total-Energy Calculations Using a Plane-Wave Basis Set. *Phys. Rev. B: Condens. Matter Mater. Phys.* **1996**, *54*, 11169–11186.

(36) Perdew, J. P.; Burke, K.; Ernzerhof, M. Generalized Gradient Approximation Made Simple. *Phys. Rev. Lett.* **1996**, *77*, 3865–3868.

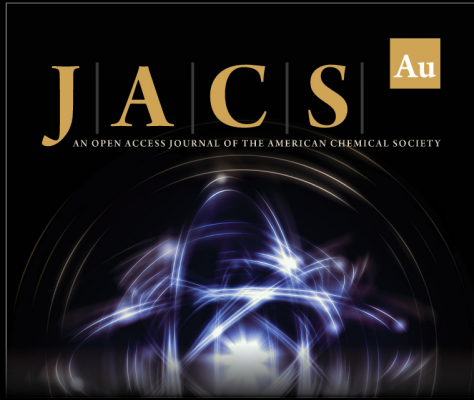
(37) Lee, K.; Murray, E. D.; Kong, L.; Lundqvist, B. I.; Langreth, D. C. Higher-Accuracy van Der Waals Density Functional. *Phys. Rev. B: Condens. Matter Mater. Phys.* **2010**, *82*, 081101.

(38) Kühne, T. D.; Iannuzzi, M.; Del Ben, M.; Rybkin, V. V.; Seewald, P.; Stein, F.; Laino, T.; Khaliullin, R. Z.; Schütt, O.; Schiffmann, F.; Golze, D.; Wilhelm, J.; Chulkov, S.; Bani-Hashemian, M. H.; Weber, V.; Borštnik, U.; TAILLEFUMIER, M.; Jakobovits, A. S.; Lazzaro, A.; Pabst, H.; Müller, T.; Schade, R.; Guidon, M.; Andermatt, S.; Holmberg, N.; Schenter, G. K.; Hehn, A.; Bussy, A.; Belleflamme, F.; Tabacchi, G.; Glöb, A.; Lass, M.; Bethune, I.; Mundy, C. J.; Plessl, C.; Watkins, M.; VandeVondele, J.; Krack, M.; Hutter, J. CP2K: An Electronic Structure and Molecular Dynamics Software Package -Quickstep: Efficient and Accurate Electronic Structure Calculations. *J. Chem. Phys.* **2020**, *152*, 194103 AIP Publishing LLC AIP Publishing May.


(39) Nosé, S. A Unified Formulation of the Constant Temperature Molecular Dynamics Methods. *J. Chem. Phys.* **1984**, *81*, 511–519.


(40) VandeVondele, J.; Hutter, J. Gaussian Basis Sets for Accurate Calculations on Molecular Systems in Gas and Condensed Phases. *J. Chem. Phys.* **2007**, *127*, 114105.


(41) Goedecker, S.; Teter, M.; Hutter, J. Separable Dual-Space Gaussian Pseudopotentials. *Phys. Rev. B* **1996**, *54*, 1703–1710.



JACS Au
AN OPEN ACCESS JOURNAL OF THE AMERICAN CHEMICAL SOCIETY

 Editor-in-Chief
Prof. Christopher W. Jones
Georgia Institute of Technology, USA

Open for Submissions 

pubs.acs.org/jacsau  ACS Publications
Most Trusted. Most Cited. Most Read.